Rb_3InCl_6 – A Monoclinic Double Perovskite Derivative with Bright Sb^{3+}-Activated Photoluminescence

*Jackson D. Majher[†], Matthew B. Gray[†], Tianyu Liu[†], Noah P. Holzapfel[†], and Patrick M. Woodward[†]**

[†]Department of Chemistry and Biochemistry, The Ohio State University, 100 W. 18th Avenue, Columbus, OH, 43210, United States

ABSTRACT: Here we present the synthesis and crystal structure of Rb_3InCl_6 prepared from air stable reagents via a two-step process that proceeds through the intermediate $Rb_2InCl_5 \cdot H_2O$. Rb_3InCl_6 crystallizes with the Rb_3YCl_6 structure type (*C*2/*c*), which can be derived from the double perovskite structure by noncooperative tilting of isolated $[InCl_6]^{3-}$ octahedra. Despite this lowering of symmetry, the optical properties are similar to the cubic double perovskite $Cs_2NaInCl_6$. Partial substitution of In^{3+} with Sb^{3+} in Rb_3InCl_6 results in intense cyan-green photoluminescence originating from localized $5s^2$ to $5s^15p^1$ electronic transitions of $[SbCl_6]^{3-}$ polyatomic anions. Compared with the cubic double perovskite phosphor $Cs_2NaInCl_6:Sb^{3+}$, the octahedral tilting distortion increases the electronic isolation of the In/Sb-centered octahedra thus facilitating electron and hole localization on Sb^{3+} sites, leading to bright photoluminescence. The distorted crystal structure also leads to a larger Stokes shift (1.29 eV) and a corresponding red shift of the emission peak (λ_{max} = 522 nm) compared to the more symmetric $Cs_2NaInCl_6:Sb^{3+}$ (Stokes shift ≈ 0.94 eV, λ_{max} = 445 nm).

INTRODUCTION:

Halide perovskites with formula ABX_3 ($A = Cs^+$, $NH_3CH_3^+$; $B^{2+} = Pb^{2+}$, Sn^{2+}; $X = Cl^-$, Br^-, I^-) have been heavily researched due to their exceptional optoelectronic properties. Besides their immense potential for solar energy conversion, their luminescent properties have become an area of intense research. For example, quantum confined perovskite nanocrystals can be made with high efficiency narrowband emission throughout the visible range, tunable by varying the anion composition.[1-3] This discovery has since led to advances in harnessing the electroluminescence of these materials in light emitting diodes (LEDs).[4] However, the photoluminescent properties of $APbX_3$ and $ASnX_3$ perovskites have some limitations. The lack of quantum confinement and the small exciton binding energy leads to short lived excitons and that tends to reduce the probability of radiative recombination. Lower dimensional perovskite derivatives such as zero-dimensional (0-D) perovskites with isolated $[PbX_6]^{4-}$ and $[SnX_6]^{4-}$ octahedra confine the excited state to a single octahedron, thus boosting photoluminescence (PL) by reducing exciton dissociation.[5,6] Cs_4PbBr_6, Cs_4SnBr_6, $(TDMP)_6Pb_3Br_{12}$ (TDMP = *trans*-2,5-dimethylpiperazine), and $(C_4N_2H_{14}Br)_4SnBr_6$ are all examples of such materials that exhibit notable PL properties.[7-10]

Halide double perovskites, $A_2B^IB^{III}X_6$ ($A = Cs^+$, Rb^+; $B^I = Na^+$, Ag^+; $B^{III} = In^{3+}$, Sb^{3+}, Bi^{3+}; $X = Cl^-$, Br^-) are site ordered variants of the ABX_3 structure, with B^I and B^{III} occupying the octahedral sites in a rock salt pattern.[11-14] Despite their three-dimensional structure, compositions where B^I is an alkali metal cation, including $Cs_2NaInCl_6$ and $Cs_2NaBiCl_6$, effectively possess a "0-D electronic structure" due to the large energy mismatch of the valence orbitals on the B^I and B^{III} ions.[15] These systems possess large band gaps, strong electron-phonon coupling, and a reduced electronic dimensionality that aid in the trapping of excitons, either on dopant sites (i.e. Sb^{3+}, Mn^{2+}, Eu^{3+}) or through distortions of the lattice leading to the formation of self-trapped excitons (STE).[16-26] For

example, the vacancy ordered double perovskites $Cs_2SnCl_6:Bi^{3+}$ and $Cs_2SnCl_6:Sb^{3+}$ exhibit blue and orange photoluminescence, respectively.[27-30] $Cs_2NaInCl_6$ doped with Sb^{3+} exhibits intense blue luminescence (λ_{max} = 445 nm; PLQY = 79%) originating from the $^3P_1 \rightarrow {}^1S_0$ transition of Sb^{3+}.[16-18]

The replacement of Group IV elements with In^{3+} leads to a reduction in the toxicity with respect to materials that contain Pb^{2+} and enhanced oxidative stability in comparison to those that contain Sn^{2+}. $Rb_2InCl_5 \cdot H_2O$ doped with Sb^{3+} has been reported as an orange emitting phosphor ($\lambda_{max} \approx 600$ nm; PLQY = 90%), while $Cs_2InCl_5 \cdot H_2O$ doped with Sb^{3+} emits in the yellow (λ_{max} = 580 nm; PLQY = 95%), both are electronically and structurally 0-D in nature.[31-33] The shift from blue emission in $Cs_2NaInCl_6:Sb^{3+}$ to orange emission in $Rb_2InCl_5 \cdot H_2O:Sb^{3+}$ is a result of the change from a $[SbCl_6]^{3-}$ activator in the former to a $[SbCl_5(H_2O)]^{2-}$ activator in the latter. The lower symmetry and relatively weak dative bond between Sb^{3+} and H_2O permit more structural reorganization of the excited state and a larger Stokes shift.

A recent study found that highly efficient PL (λ_{max} = 497 nm; PLQY = 95%) can be obtained by doping Sb^{3+} ions into a Rb_3InCl_6 host.[33] Although exceptional PL properties of $Rb_3InCl_6:Sb^{3+}$ have been identified, many important features of this phosphor are not well understood. In particular, the cubic double perovskite crystal structure reported in the Supporting Information of ref 33 is not consistent with the complexity of the X-ray powder diffraction pattern. Knowledge of the crystal structure and the corresponding host site environment of Sb^{3+} is necessary for understanding the photophysical properties of this promising material. Details of the crystal structure may help to explain why this compound emits at longer wavelengths than the double perovskite $Cs_2NaInCl_6:Sb^{3+}$, even though octahedral $[SbCl_6]^{3-}$ groups are thought to play the role of sensitizer and activator in both compounds. Those issues are examined and answered in this

paper. Furthermore, an alternative synthesis route for Rb_3InCl_6 using a simple two-step method is identified. This enables efficient synthesis of phase pure samples from air stable reagents, an important advance for potential applications of this material.

EXPERIMENTAL:

RbCl (RPI, 99.9%), In_2O_3 (Alfa Aesar, 99.994%), Sb_2O_3 (Acros Organics, 99+%), hydrochloric acid (Fisher Scientific, 37%), hypophosphorous acid (Sigma Aldrich, 50 wt. % in H_2O), ethanol (Decon Labs Inc., 200 proof), methanol (Fisher Scientific, 99.8%), and acetonitrile (Fisher Scientific, 99.9%) were all used as received.

$Rb_2InCl_5 \cdot H_2O$ was prepared by a similar method to that reported previously.[32] For a typical synthesis, 1 mmol In_2O_3 was added to hydrochloric acid (5 mL) and stirred until the solution became clear. Then 4 mmol of RbCl was added to precipitate $Rb_2InCl_5 \cdot H_2O$ as a white powder. To incorporate Sb^{3+}, a variable amount of Sb_2O_3 (0-1 mmol) was dissolved in the HCl(aq) solution prior to triggering precipitation and hypophosphorous acid (1 mL) was added to prevent oxidation of Sb^{3+}. All products were dried via vacuum filtration and washed with ethanol.

Rb_3InCl_6 was prepared by adding 1 mmol of $Rb_2InCl_5 \cdot H_2O$ to 20 mL of acetonitrile and sonicating for 10 minutes. The resulting product was filtered and washed with acetonitrile. Sb^{3+} doped $Rb_2InCl_5 \cdot H_2O$ samples appear to fully retain antimony upon conversion to Rb_3InCl_6. Heating the solution was found to increase the rate of transformation, and the use of fresh solvents improves the efficiency of conversion.

Single crystals of Rb_3InCl_6 were grown by using previously synthesized Rb_3InCl_6 powder. For a typical synthesis, 0.2 mmol of Rb_3InCl_6 was added to 10 mL of methanol and sealed in a Teflon-

lined Parr reactor. The vessel was placed in a box furnace and heated to 120 °C and held for 10 hours. The oven was then slowly cooled at 1 °C/hr to yield plate-like crystals of Rb_3InCl_6.

Powder X-ray diffraction (PXRD) data were collected on a Bruker D8 Advance powder diffractometer (40 kV, 40 mA, sealed Cu X-ray tube) equipped with a Lynxeye XE-T position-sensitive detector. The data were collected with an incident beam monochromator (Johansson type SiO_2-crystal) that selects only Cu $K_{\alpha 1}$ radiation (λ = 1.5406 Å). Rietveld refinements of laboratory PXRD data were carried out using the TOPAS-Academic (Version 6) software package to determine the crystal structure.[34] Crystal structure images were generated with Vesta 3.[35]

Single-crystal XRD (SCXRD) studies were carried out on a Nonius Kappa diffractometer equipped with a Bruker APEX-II CCD and Mo Kα radiation (λ = 0.71073 Å). A 0.333 × 0.207 × 0.048 mm colorless crystal was mounted on a MiTeGen MicroMount with clear enamel. Data were collected at ambient conditions using ω-scans. The crystal-to-detector distance was 60 mm, and the exposure time was 10 s per frame using a scan width of 0.8°. A total of 13774 reflections were collected covering the indices, $-31 \leq h \leq 31$, $-9 \leq k \leq 9$, $-15 \leq l \leq 9$. The number of symmetry independent reflections was 2515. The data were integrated using the Bruker SAINT software program and scaled using the SADABS software program. Solution by direct methods (SHELXT) produced a complete phasing model for refinement. All atoms were refined with anisotropic displacement parameters via full-matrix least squares (SHELXL-2014).

UV-visible diffuse reflectance spectroscopy (DRS) data were collected from 178–890 nm with an Ocean Optics USB4000 spectrometer equipped with a Toshiba TCD1304AP (3648-element linear silicon CCD array). The spectrometer was used with an Ocean Optics DH-2000-BAL deuterium and halogen UV−vis−NIR light source and a 400 μm R400-7-ANGLE-VIS reflectance probe. The detector was calibrated using a Spectralon Diffuse Reflectance Standard. Steady-state

photoluminescence data were obtained using a Jovin Horiba FluoroMax4 (Xenon source, 0.75 nm excitation and emission slit widths, 1 nm step size) equipped with a solid-state sample holder. Luminescent data was analyzed using the FluorEssence (v3.5) software powered by Origin.

Thermogravimetric analysis (TGA) was performed on a Thermogravimetric Analyzer TGA Q50. Samples were heated under a nitrogen stream of 50 mL/minute with a heating rate of 10 °C/minute between 25 °C and 800 °C.

RESULTS:

Synthesis of Rb_3InCl_6 was achieved through a two-step process. First, the hydrate phase $Rb_2InCl_5 \cdot H_2O$ was prepared in hydrochloric acid through a precipitation reaction. Second, the hydrate phase was converted to Rb_3InCl_6 by sonication in acetonitrile. Variable addition of Sb_2O_3 (0-100 mol%) in the HCl(aq) solution results in low levels (~1-2 mol%) of Sb^{3+} incorporation on the octahedral sites of the hydrate phase and the Sb^{3+} is retained upon transformation to Rb_3InCl_6.[32] In the Sb^{3+} doped samples the conversion from $Rb_2InCl_5 \cdot H_2O$ to Rb_3InCl_6 can be monitored by following the change in the color of the PL from orange to cyan-green under UV excitation (Figure S2).

Using tools in the software package TOPAS, the PXRD pattern of Rb_3InCl_6 synthesized in the above manner was indexed to a monoclinic unit cell with approximate lattice parameters a = 12.52 Å, b = 7.78 Å, c = 13.20 Å and β = 108.17˚. The indexed unit cell parameters were searched against the library of known phases in the ICSD, and K_3MoCl_6 was identified as a prospective isostructural analog based upon similarities in the unit cell parameters and stoichiometry. A Rietveld refinement of the PXRD data for Rb_3InCl_6 using the K_3MoCl_6 structure (space group = $P2_1/a$) as a starting point provided a good fit, though the large number of variables made it difficult to obtain a

chemically reasonable structure. SCXRD analysis found a closely related structure with *C*2/*c* symmetry (Rb_3YCl_6 structure type) and unit cell dimensions of a = 25.449(2) Å, b = 7.7836(5) Å, c = 12.5571(9) Å, α = 90º, β = 99.771(2)º, γ = 90º (see Table S1). Refinement of SCXRD resulted in a final R1 = 0.0329 (I > 2σ(I)) and wR2 = 0.0860. A Rietveld refinement of powder data using the structural data obtained for the Rb_3InCl_6 single crystal gave an improved fit, R_{wp} = 9.348% with the *C*2/*c* structure (see Figure 1) vs. 10.949% with the $P2_1/a$ structure, confirming the *C*2/*c* solution. Given the fact that both structures have the same number of atoms in the asymmetric unit, and hence the same number of variables to define the structure, this improvement in fit provides further support for the assignment of *C*2/*c* symmetry. The full refinement details along with the crystallographic information file are included in the Supporting Information.

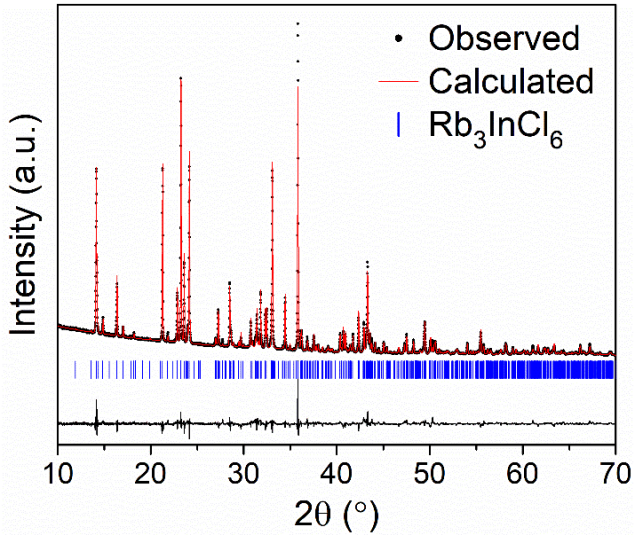

Figure 1. Rietveld refinement of Rb_3InCl_6. The observed data, calculated fit, and difference curve are shown with black dots, a red line, and a black line, respectively.

This structure may be visualized as a distorted variant of the cubic double perovskite structure with formula $A_2B^IB^{III}X_6$ (i.e. $Rb_2RbInCl_6$) through rotations of the octahedral $[BX_6]^{3-}$ units. As seen in Figure 2, the $[InCl_6]^{3-}$ octahedra on the 4e Wyckoff site all have the same orientation.

These may be viewed as retaining the orientation found in the parent cubic double perovskite structure. The remaining ½ of the $[InCl_6]^{3-}$ octahedra (4c Wyckoff site) are tilted by approximately 45º about two of the three internal fourfold axes thus breaking the 3-D corner connected arrangement of octahedra in a hypothetical $Rb_2RbInCl_6$ cubic double perovskite structure (Figure 2). The octahedral tilts lead to relatively small distortions from the ideal octahedral coordination of In seen in the cubic double perovskite structure (see Table 1).

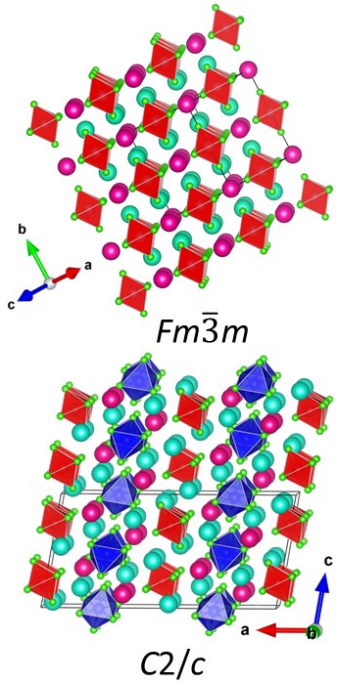

Figure 2. A comparison of the hypothetical cubic Rb_3InCl_6 structure (top) and the actual monoclinic structure of Rb_3InCl_6. The $[InCl_6]^{3-}$ octahedra that retain the orientation of the cubic structure are shown in red (Wyckoff site 4e) and those that are tilted by ~45° from the cubic orientation are shown in blue (Wyckoff site 4c). Rb^+ ions that reside on the B^I site of the double perovskite structure are represented with pink spheres and those that occupy the A site with cyan spheres.

Table 1. List of bond lengths and angles of the two $[InCl_6]^{3-}$ environments in Rb_3InCl_6.

Bond length (Å)	
In(1)−Cl(1)	2.528(1)
In(1)−Cl(2)	2.525(1)
In(1)−Cl(3)	2.501(1)
In(2)−Cl(4)	2.540(1)
In(2)−Cl(5)	2.480(1)
In(2)−Cl(6)	2.524(1)
Angle (°)	
Cl(1)−In(1)−Cl(2)	90.46(4)
Cl(1)−In(1)−Cl(3)	90.06(5)
Cl(2)−In(1)−Cl(3)	86.48(5)
Cl(4)−In(2)−Cl(5)	89.58(5)
Cl(4)−In(2)−Cl(6)	91.33(5)
Cl(5)−In(2)−Cl(6)	90.95(5)

As a result of the octahedral tilting, the Rb^+ ions which would normally sit on the 6-coordinate B^I octahedral site experience an increase in coordination number to 8, whereas the A-site Rb^+ cations undergo a reduction in coordination from the 12-coordinate environment of the cubic double perovskite to either an 8- or 11-coordinate environment (Figure S3). Because of the increase in the coordination number of the B^I site this distortion has been called noncooperative octahedral tilting.

The perfection with which a given set of ions fit together in the cubic perovskite structure can be expressed by the Goldschmidt tolerance factor,[37]

$$t = \frac{r_A + r_x}{\sqrt{2}(r_B + r_x)}, \qquad (1)$$

where r_A, r_B, and r_x are the average radii of the ions that make up the ABX_3 formula, and t is the tolerance factor. When $t = 1$, the ions fit together perfectly in the cubic structure. Noncooperative octahedral tilting tends to occur in systems with a low tolerance factor ($t \leq 0.93$) and large size mismatch between the B^I and B^{III} ions.[38] Bond valence sum analysis (Table S3) shows that

noncooperative tilting removes the severe under-bonding of A-site Rb^+ cations which would occur in the hypothetical cubic double perovskite structure (t = 0.84 for Rb_3InCl_6). The rubidium bond valence sums are 1.24, 1.34, and 0.82 for the Rb^+ ions sitting at the 8-coordinate site B^-site, the 8-coordinate A-site, and the 11-coordinate A-site, respectively.

Diffuse reflectance spectroscopy (DRS) measurements were collected on powder samples and converted to pseudo-absorbance through the Kubelka Munk transformation as given in equation 2:

$$\alpha = \frac{(1-R)^2}{2R}, \qquad (2)$$

where α is the optical absorption coefficient and R is reflectance. As seen in Figure 3, the onset of absorption in undoped Rb_3InCl_6 occurs at 237 nm (5.22 eV). The large band gap is not surprising as the large separation of $[InCl_6]^{3-}$ octahedra results in minimal overlap between molecular orbitals on neighboring polyatomic anions, leading to a 0-D electronic structure.

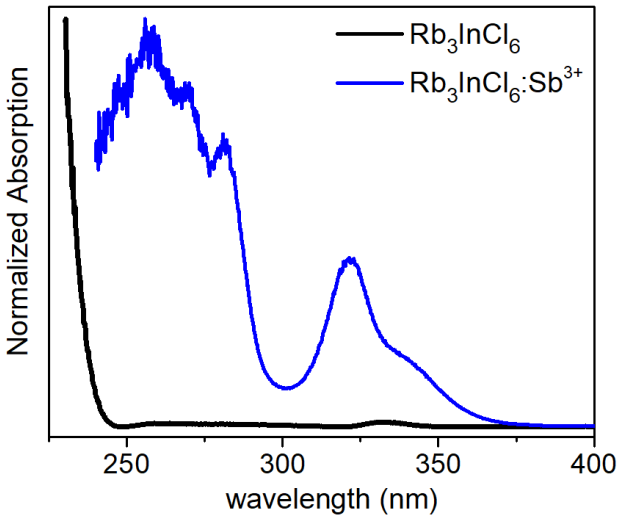

Figure 3. Kubelka-Munk transformation of diffuse reflectance spectra of Rb_3InCl_6 with (blue) and without Sb^{3+} (black) doping.

Once Sb^{3+} ions are incorporated a number of near-UV absorption features are observed. These features are characteristic of optical excitations that are associated with the s^2 to s^1p^1 transitions of p-block ions with a filled valence ns^2 subshell (Tl^+, Pb^{2+}, Sb^{3+}, etc.).[39,40] The broad absorption feature centered at 265 nm is assigned to the spin and parity allowed $^1S_0 \rightarrow {}^1P_1$ transition (C band). The B band, positioned at 285 nm, is assigned to the parity and spin forbidden $^1S_0 \rightarrow {}^3P_2$ transition, which appears because vibronic coupling and spin-orbit coupling relax the selection rules. Lastly, the doublet with peaks at 321 and 342 nm corresponds to the parity allowed, spin forbidden $^1S_0 \rightarrow {}^3P_1$ transition (A band). This transition is partially allowed due to spin-orbit coupling induced mixing of the $^1P_1$ and $^3P_1$ states. The absorption peak is split due to a dynamic Jahn-Teller (JT) distortion of the excited state, which couples to lattice vibrations. The spacing and positions of these transitions is consistent with that expected from literature and nearly identical to the absorption features that arise when Sb^{3+} ions are doped into $Cs_2NaInCl_6$ (Figure S4).[16,39,41]

Rb_3InCl_6 samples doped with Sb^{3+} exhibit bright luminescence, most accurately described as "aquamarine" to the naked eye. To study this quantitatively, photoluminescent measurements were taken (see Figure 4). The peaks in the excitation spectrum correspond closely to those seen in the UV absorption spectrum (Figure S5), leaving little doubt that Sb^{3+} acts as both the sensitizer and the activator. The excitation spectrum below 300 nm is instructive. There is a peak in the excitation spectrum that falls close to the 285 nm peak seen in the absorption spectrum, but no clear feature in the 250-270 nm region where the diffuse reflectance spectrum shows intense absorbance (Figure 3). This supports the assignment of the 285 nm peak to the $^1S_0 \rightarrow {}^3P_2$ transition, because no intersystem crossing would be required to produced luminescence from the $^3P_2$ excited state, unlike the $^1P_1$ excited state. The emission of Rb_3InCl_6:Sb^{3+} has a maximum at 522 nm with a FWHM of

129 nm (59.7 meV) and CIE coordinates (0.247,0.394). The Stokes shift of 1.29 eV lies between that of $Cs_2NaInCl_6:Sb^{3+}$ (0.94 eV) and $Rb_2InCl_5 \cdot H_2O:Sb^{3+}$ (2.1 eV).[16,32]

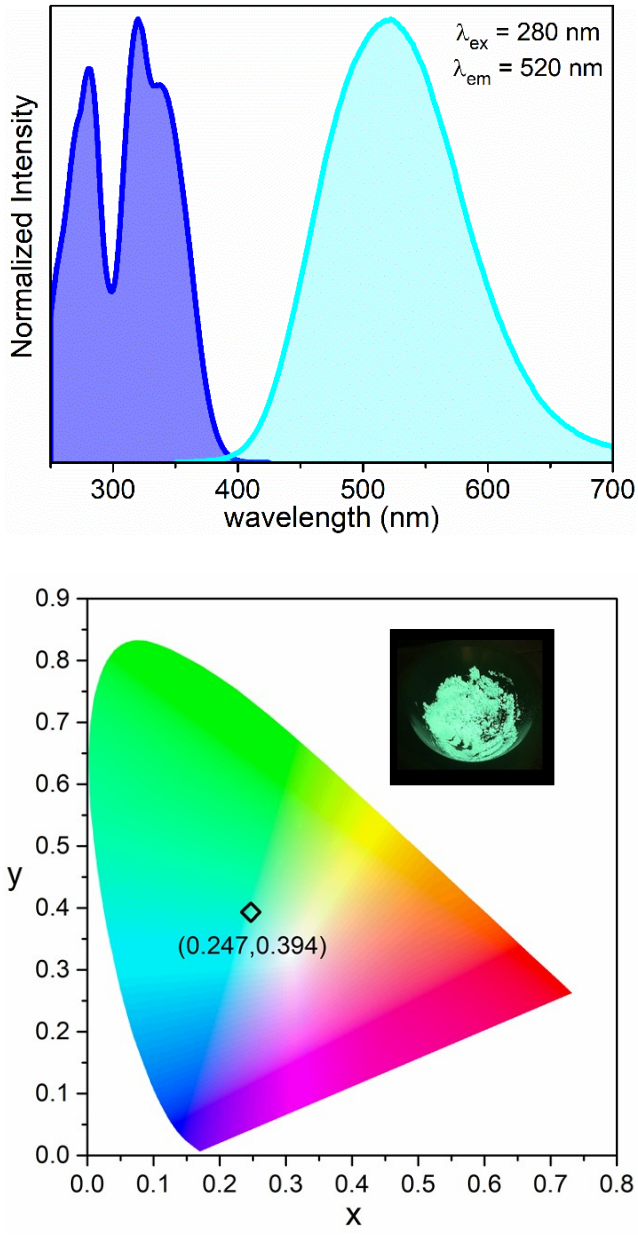

Figure 4. Top: Excitation (blue) and emission (cyan) of Sb^{3+} doped Rb_3InCl_6. Bottom: CIE diagram (1931) of $Rb_3InCl_6:Sb^{3+}$. The inset shows a photo of $Rb_3InCl_6:Sb^{3+}$ under UV excitation.

The thermal and chemical stability of Rb_3InCl_6 are important characteristics for optoelectronic applications. TGA measurements (Figure S7) show excellent thermal stability of Rb_3InCl_6 with

decomposition occurring at 550 °C. PXRD scans taken after 100 days storage in air indicate no degradation of the phase (Figure S8). The excellent stability of this phase in ambient air is consistent with earlier reports which observed no decomposition after 5 months of exposure to air.[33] Furthermore, photoluminescence was found to be stable over 100 days (Figure S9), an important feature for phosphor applications.

DISCUSSION:

Among halide double perovskites the synthesis of Rb_3InCl_6 is distinct from the much more common approach of precipitation from aqueous hydrohalic acid. With the exception of $Cs_2NaInCl_6$ and $Cs_2AgInCl_6$, attempted syntheses of other halide double perovskite phases containing In^{3+} in hydrohalic acid results in the formation of $A_2InX_5 \cdot H_2O$ ($A = Cs^+, Rb^+$; $X = Cl^-, Br^-$) hydrate phases. Synthetic routes using nonaqueous organic solvents are less explored and the results reported here support further investigation into these methods. Whereas concentrated HCl contains approximately 64% H_2O by mass, nonaqueous solvents provide an equilibrium that can inhibit formation of the hydrated product. The transformation of the hydrate phase to Rb_3InCl_6 is thought to proceed by the following reaction in acetonitrile:

$$3\ Rb_2InCl_5 \cdot H_2O(s) \rightleftharpoons 2\ Rb_3InCl_6(s) + InCl_3(solv) + 3\ H_2O(solv). \qquad (3)$$

$InCl_3$ stays dissolved in solution whereas Rb_3InCl_6 remains in the solid state due to its limited solubility. The differences in solubility of RbCl and $InCl_3$ in acetonitrile, together with the miscibility between water and acetonitrile, drives the equilibrium expressed in equation 3 toward the product side. Other solvents were investigated for the conversion of $Rb_2InCl_5 \cdot H_2O$ to Rb_3InCl_6 using the color differences in the PL of the two phases to track the extent of the reaction. Evidence

for this transformation was also observed in methanol, ethanol, and acetone whereas solvents such as isopropanol, diethyl ether, and hexanes resulted in no observed conversion. Prior research on hybrid organic-inorganic indium halide phases demonstrates that in addition to solvent choice, product formation is sensitive to the concentration of the precursor reagents.[42] It is likely that similar synthetic routes may be developed for the conversion of other hydrate phases.

It should be noted that the synthesis reported in this work is considerably simpler than the reaction conditions previously employed to prepare $Rb_3InCl_6:Sb^{3+}$, which included elevated temperatures (130 °C) and relatively long reaction times (>30 hours) involving costly, air sensitive reagents.[33] As the hydrate precursor is readily made in HCl(aq) at room temperature, no heat is needed for formation of Rb_3InCl_6. Because HCl acts as the chloride source, air-sensitive reagents such as $InCl_3$ and $SbCl_3$ can be replaced by the corresponding oxides, eliminating the need for an inert atmosphere. Formation of the hydrate is fast, due to the exceptional solubility of In_2O_3 in HCl and transformation of the hydrate to Rb_3InCl_6 in acetonitrile occurs in 10 minutes, greatly reducing synthesis times. These features improve the feasibility of large-scale production of this material improving its potential for commercial use.

Although this is the first report of the crystal structure of Rb_3InCl_6, the structures of numerous A_3BX_6 halides are derived from the double perovskite structure by noncooperative octahedral tilting. Benachenhou et al. devised a useful system for relating all of these structures to each other and to the cubic double perovskite by visualizing the $[BX_6]^{3-}$ octahedra in these structures as large spheres that take on a cubic close packed arrangement.[43] The charge balancing A^+ ions reside in either the octahedral or tetrahedral holes within the close packed arrangement of polyatomic anions (Figure S11). For a cubic double perovskite, with formula $A_2B'BX_6$, the cubic close packing occurs along the body diagonal of the unit cell, with the B′ site cation occupying the octahedral

holes and the A site cations occupying the tetrahedral holes. In all structural variants the octahedral and tetrahedral holes are filled, leading to the $A_2B'BX_6$ stoichiometry (Table S4).

Noncooperative titling in halide perovskites leads to several crystal structures, which may be grouped according to the fraction of $[MX_6]^{3-}$ octahedra that tilt away from their orientation in the cubic structure. Tables S4 and S5 provides a representative list of compounds. Tetragonal structures are the most closely related to the cubic double perovskite structure. Only one in five octahedra are rotated, each by ~45º about one of the fourfold axes of the octahedron.[44] For compositions adopting the monoclinic space groups with either $P2_1/a$ or $C2/c$ symmetry, 50% of octahedra are titled, each by ~45º about two of the fourfold axes. The orthorhombic structures (*Pnma*, *Pbcm*) are further distorted with 75% of the octahedra being tilted away from the cubic perovskite orientation (Figure S12). In oxide and fluoride structures with noncooperative tilting, successive phase transitions lead to a reduction in the fraction of tilted octahedra as the temperature increases until the cubic structure is reached.[45-47] It is unknown whether such phase transitions occur for A_3BX_6 and $A_2B'BX_6$ compounds with heavier halide ions, as very few studies on the temperature dependent phase transitions in these systems have been reported.[44,48,49]

In order to understand the optical properties of $Rb_3InCl_6:Sb^{3+}$ it is instructive to compare them to those of the cubic double perovskite $Cs_2NaInCl_6:Sb^{3+}$. The absorption onset of Rb_3InCl_6 occurs at slightly higher energy (5.22 eV) than $Cs_2NaInCl_6$ (5.09 eV) as seen in Figure S6. Due to the electropositive nature of the A and B^I ions, both hosts possess a 0-D electronic structure with a wide gap between the largely nonbonding Cl 3p valence bands and the antibonding In 5s–Cl 3p conduction band. In the limit of very large separation of $[InCl_6]^{3-}$ octahedra, there is no overlap between the molecular orbitals on neighboring octahedra, leading to flat bands and a perfectly 0-D electronic structure.[15,17,23] While this is a reasonably good approximation for $Cs_2NaInCl_6$, band

structure calculations show slight curvature at Γ corresponding to the weak bonding interactions between the In 5s–Cl 3p LUMOs on neighboring octahedra (see Figure S13).[17,23] The substantial octahedral tilts seen in Rb_3InCl_6 reduce this overlap, further narrowing the conduction band with respect to $Cs_2NaInCl_6$ or vacancy ordered cubic double perovskites like Cs_2SnCl_6.

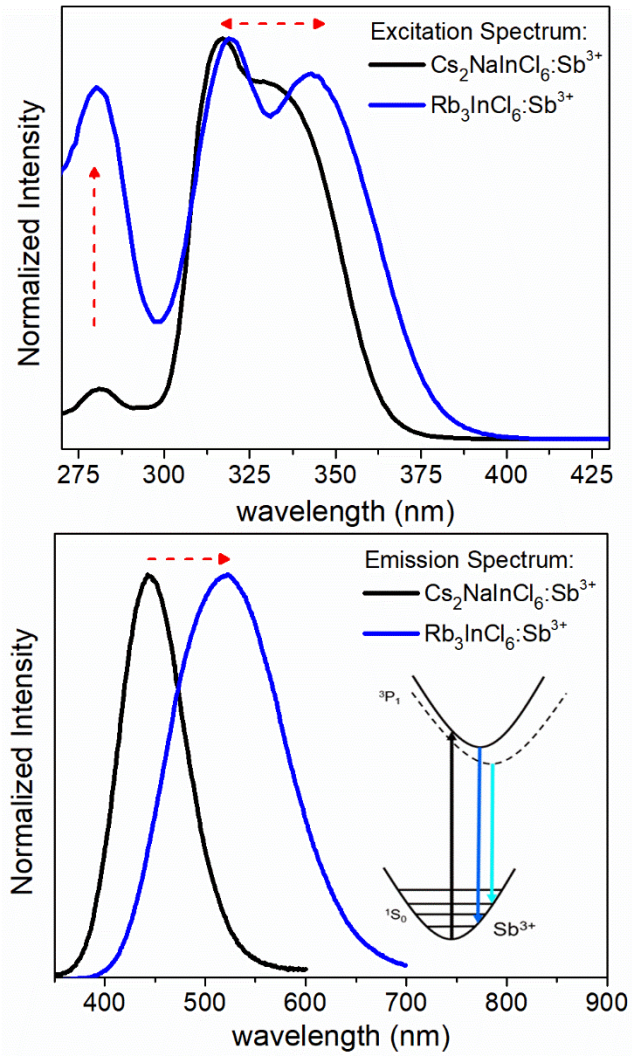

Figure 5. Comparison of excitation profile (top) and emission profile (bottom) of Sb^{3+} doped $Cs_2NaInCl_6$ and Rb_3InCl_6. Inset: Energy diagram of observed PL process.

Upon doping Sb^{3+} into the lattice, mid-gap states are introduced corresponding to the $5s^2$ to $5s^15p^1$ transitions of Sb^{3+}. The observed absorption bands of Sb^{3+} occur at similar energies in

Rb_3InCl_6 and $Cs_2NaInCl_6$, due to the similarities of the first coordination shell of Sb^{3+}. Comparing excitation profiles (Figure 5), it can be seen that both possess a high energy excitation band corresponding to the $^1S_0 \rightarrow {}^3P_2$ (B band) and a lower energy band $^1S_0 \rightarrow {}^3P_1$ (A band) that is split into two peaks by electron-phonon (vibronic) coupling of the excited state through a dynamic JT effect. However, the two spectra are not identical. In Rb_3InCl_6 the intensity of the B band is enhanced, and the splitting of the A band is increased. The larger JT splitting of the excitation spectrum of Rb_3InCl_6:Sb^{3+} implies a larger degree of electron-phonon coupling compared to the cubic structure.[39] This may also explain the increased intensity of the B-band, which becomes partially allowed through coupling to lattice vibrations. The emission peak is red-shifted and broadened in Rb_3InCl_6:Sb^{3+} compared to $Cs_2NaInCl_6$:Sb^{3+}, consistent with a larger Stokes shift. A detailed look at the crystal structures of the two compounds helps explain this observation. Rb_3InCl_6 contains two $[InCl_6]^{3-}$ sites with polyhedral volumes of 21.17(2) $Å^3$ and 21.24(2) $Å^3$ whereas there is only one $[InCl_6]^{3-}$ site in $Cs_2NaInCl_6$, and it has a smaller volume of 20.45(9) $Å^3$. The larger octahedral volume in Rb_3InCl_6 and slight distortion of the sites facilitates increased reorganization of the excited state leading to a larger Stokes shift.[49,50] Furthermore, octahedral titling in the monoclinic structure both lengthens and increases the number of Rb–Cl bonds, weakening the bonding interactions that oppose excited-state distortions of the $[SbCl_6]^{3-}$ octahedra. This should result in a larger degree of electron-phonon coupling.

Efficient luminescence in halide double perovskites has been attributed to low electronic dimensionality and strong electron-phonon coupling. Low electronic dimensionality allows for the confinement of excitons leading to enhanced radiative recombination. In the 0-D structure, excitons are effectively confined to a single octahedron. In the case of Rb_3InCl_6:Sb^{3+}, the absorption and subsequent emission are localized on $[SbCl_6]^{3-}$ octahedra. This facilitates high

efficiency radiative recombination leading to the impressive reported photoluminescent quantum yield of 95%.[33] Previous analysis of similar systems has led to the assignment of PL from self-trapped excitons. Although the exciton is confined to the Sb^{3+} site, the descriptor of STE implies the existence of free excitons which we believe is not applicable in these materials. Taken together, the reduced electronic dimensionality and strong electron-phonon coupling of $Rb_3InCl_6:Sb^{3+}$ help to explain the near unity quantum efficiency of this material.

As previously mentioned, 0-D halide double perovskites comprise a large family of compounds. The photoluminescence properties of these compounds have been largely unexplored. To the best of our knowledge, $Cs_3LaX_6:Ce^{3+}$ (X = Cl^-, Br^-, I^-), previously studied for scintillation applications, is the only example of such research.[52] The results given here demonstrate the great potential of these systems, as they possess many favorable attributes including a large band gap, a 0-D electronic structure, and strong electron-phonon coupling. Both the size and distortion of the dopant site also are important factors in predicting the corresponding PL properties. Table 2 lists a variety of other reported 0-D halide double perovskites likely to be suitable phosphor hosts. The emission characteristics of these hosts doped with activator ions like Sb^{3+} are expected to be highly dependent on the octahedral volume of the trivalent host site, with a larger volume allowing for more excited state rearrangement and thus a larger Stokes shift. The A and B^I ions also determine in large part the softness of the lattice, thereby influencing the excited state distortion of ns^2 ions. For compounds with high ionicity, sensitivity to moisture may prove limiting for some compositions and should be considered. Solid solutions of 0-D halide double perovskites may serve to further tune PL allowing for specific tailoring of optical properties. Further analysis of these systems may prove valuable for applications such as phosphor converted LED lighting, scintillators, optical thermography, and IR optical communication.

Table 2. Reported 0-D halide perovskites with size and distortion of the $[BX_6]^{3-}$ site.

Formula	Space group	Average $[MCl_6]^{3-}$ volume (Å^3)	Ref.
K_3TiCl_6	*P*2$_1$/*a*	18.54	*53*
K_3ScCl_6	*P*2$_1$/*a*	20.20	*54*
Cs_3ScCl_6	*C*2/*c*	20.58	*55*
K_3InCl_6	*P*2$_1$/*a*	20.60	*56*
Rb_3InCl_6	***C*2/*c***	**21.21**	***this work***
Rb_3YCl_6	*C*2/*c*	24.13	*57*
Cs_3YCl_6	*Pbcm*	25.56	*57*
Cs_3BiCl_6	*C*2/*c*	26.20	*43*
Cs_3LaCl_6	*C*2/*c*	28.01	*58*
Rb_3BiBr_6	*Pnma*	30.71	*59*
Cs_3BiBr_6	*C*2/*c*	30.74	*60*

CONCLUSION:

Rb_3InCl_6 is shown to crystallize with the Rb_3YCl_6 structure with *C*2/*c* symmetry. Intense cyan-green photoluminescence is observed for samples doped with Sb^{3+}. Non-cooperative titling of octahedra electronically isolates the $[InCl_6]^{3-}$ and $[SbCl_6]^{3-}$ octahedra, thereby enhancing the luminescence of Sb^{3+} doped samples. A simple two-step, room temperature synthesis route is presented that simplifies the synthetic protocol compared to an earlier report. The relationship of Rb_3InCl_6 to other A_3MX_6 compounds suggests that further exploration of the PL properties of 0-D double perovskites with noncooperative octahedral tilting is warranted.

ASSOCIATED CONTENT

The following files are available free of charge.

(Table S1) SCXRD results. (Table S2) Wyckoff positions. (Fig. S1) Unit cell of Rb_3InCl_6. (Fig. S2) $Rb_2InCl_5{\cdot}H_2O{:}Sb^{3+}$ and $Rb_3InCl_6{:}Sb^{3+}$ under UV light. (Fig. S3) Rb^+ coordination environments. (Table S3) Bond valence analysis. (Fig. S4) Sb^{3+} doped Rb_3InCl_6 and $Cs_2NaInCl_6$ absorption comparison. (Fig. S5) Overlay of absorption and excitation. (Fig. S6) Rb_3InCl_6 and $Cs_2NaInCl_6$ absorption onset comparison. (Fig. S7) TGA of $Rb_2InCl_5{\cdot}H_2O$ and Rb_3InCl_6. (Fig. S8) Stability of Rb_3InCl_6 via XRD. (Fig. S9) Emission stability of $Rb_3InCl_6{:}Sb^{3+}$. (Fig. S10) Refinement and crystal structure of $Rb_2InCl_5{\cdot}H_2O$. (Table S4) Representative list of A_3BX_6 compounds and symmetry. (Fig. S11) Visualization of $[InCl_6]^{3-}$ cubic close packing in Rb_3InCl_6. (Table S5) Comparison of $A_2B'BX_6$ structures with non-cooperative tilting. (Fig. S12) Visualization of noncooperative tilting in $A_2B'BX_6$ structure types. (Fig. S13) Bonding interactions of $[InCl_6]^{3-}$ LUMO in $Cs_2NaInCl_6$. (PDF)

Crystallographic information file (CIF)

AUTHOR INFORMATION

Corresponding Author

*E-mail: woodward.55@osu.edu

ORCID

Jackson D. Majher: 0000-0002-4160-4201

Matthew B. Gray: 0000-0002-9526-4732

Tianyu Liu: 0000-0002-2537-4231

Noah P. Holzapfel: 0000-0002-4566-4033

Patrick M. Woodward: 0000-0002-3441-2148

Author Contributions

The manuscript was written through contributions of all authors. All authors have given approval to the final version of the manuscript.

ACKNOWLEDGEMENTS

Funding was provided by the National Science Foundation under award number DMR-2003793. Special thanks to Dr. Curtis Moore and Dr. Nicole Karn for their assistance with single crystal x-ray diffraction and TGA measurements, respectively.

Notes

The authors declare no competing financial interests.

References:

(1) Noh, J. H.; Im, S. H.; Heo, J. H.; Mandal, T. N.; Seok, S. I. Chemical Management for Colorful, Efficient, and Stable Inorganic–Organic Hybrid Nanostructured Solar Cells. *Nano Lett.* **2013,** *13,* 1764−1769.

(2) Pellet, N.; Teuscher, J.; Maier, J.; Grätzel, M. Transforming Hybrid Organic Inorganic Perovskites by Rapid Halide Exchange. *Chem. Mater.* **2015,** *27,* 2181−2188.

(3) Shamsi, J.; Urban, A.; Imran, M.; Trizio, L. D.; Manna, L. Metal Halide Perovskite Nanocrystals: Synthesis, Post–Synthesis Modifications, and Their Optical Properties. *Chem. Rev.* **2019,** *119,* 3296–3348.

(4) Le, Q. L.; Jang, H. W.; Kim, S. Y. Recent Advances toward High–Efficiency Halide Perovskite Light–Emitting Diodes: Review and Perspective. *Small* **2018,** *10,* 1700419.

(5) Seth, S.; Samanta, A. Photoluminescence of Zero–Dimensional Perovskites and Perovskite–Related Materials. *J. Phys. Chem. Lett.* **2018,** *9,* 1, 176–183.

(6) Almutlaq, J.; Yin, J.; Mohammed, O. F.; Bakr, O. M. The Benefit and Challenges of Zero–Dimensional Perovskites. *J. Phys. Chem. Lett.* **2018,** *9,* 14, 4131–4138.

(7) Saidaminov, M.; Almutlaq, J.; Sarmah, S.; Dursun, I.; Zhumekenov, A. A.; Bejum, R.; Pan, J.; Cho, N.; Mohammed, O. F.; Bakr, O. M. Pure Cs_4PbBr_6: Highly Luminescent Zero–Dimensional Perovskite Solids. *ACS Energy Lett.* **2016,** *1,* 4, 840–845.

(8) Zhang, X.; Wang, H.; Wang, S.; Hu, Y.; Liu, X.; Shi, Z.; Colvin, V. L.; Wang, S.; Yu, W. W.; Zhang, Y. Room Temperature Synthesis of All Inorganic Lead–Free Zero–Dimensional Cs_4SnBr_6 and Cs_3KSnBr_6 Perovskites. *Inorg. Chem.* **2020,** *59,* 1, 533–538.

(9) Gautier, R.; Massuyeau, F.; Galnon, G.; Paris, M. Lead–Halide Post–Perovskite–Type Chains for High–Efficiency White–Light Emission. *Adv. Mater.* **2019,** *31,* 1807383.

(10) Zhou, C.; Lin, H.; Tian, Y.; Yuan, Z.; Clark, R.; Chen, B.; van de Burgt, L. J.; Wang, J. C.; Zhou, Y.; Hanson, K.; Meisner, Q. J.; Neu, J.; Besara, T.; Siegrist, T.; Lambers, E.; Djurovich, P.; Ma, B. Luminescent zero–dimensional organic metal halide hybrids with near–unity quantum efficiency. *Chem. Sci.* **2018,** *9,* 586–593.

(11) Volonakis, G.; Haghighirad, A. A.; Milot, R. L.; Sio, W. H.; Filip, M. R.; Wnger, B.; Johnston, M. B.; Herz, L. M.; Snaith, H. J.; Giustino, F. $Cs_2InAgCl_6$: A New Lead–Free Halide Double Perovskite with Direct Band Gap. *J. Phys. Chem. Lett.* **2017,** *8,* 4, 772–778.

(12) Zhou, J.; Xia, Z.; Molokeev, M. S.; Zhang, X.; Peng, D.; Liu, Q. Composition design, optical gap and stability investigations of lead–free halide double perovskite $Cs_2AgInCl_6$. *J. Mater. Chem. A* **2017,** *5,* 15031–15037.

(13) McClure, E. T.; Ball, M. R.; Windl, W.; Woodward, P. M. Cs_2AgBiX_6 (X = Br, Cl): New Visible Light Absorbing, Lead–Free Halide Perovskite Semiconductors. *Chem. Mater.* **2016,** *28,* 5, 1348–1354.

(14) Slavney, A. H.; Hu, T.; Lindenberg, A. M.; Karunadasa, H. I. A Bismuth–Halide Double Perovskite with Long Carrier Recombination Lifetime for Photovoltaic Applications. *J. Am. Chem. Soc.* **2016,** *138,* 7, 2138–2141.

(15) Xiao, Z.; Meng, W.; Wang, J.; Mitzi, D. B.; Yan, Y. Searching for promising new perovskite–based photovoltaic absorbers: the importance of electronic dimensionality. *Mater. Horiz.* **2017,** *4,* 206–216.

(16) Gray, M. B.; Hariyani, S.; Strom, T. A.; Majher, J. D.; Brgoch, J.; Woodward, P. M. High–efficiency blue photoluminescence in the $Cs_2NaInCl_6:Sb^{3+}$ double perovskite phosphor. *J. Mater. Chem. C* **2020,** 8*,* 6797–6803.

(17) Zeng, R.; Zhang, L.; Xue, Y.; Ke, B.; Zhao, Z.; Huang, D.; Wei, Q.; Zhou, W.; Zou, B. Highly Efficient Blue Emission from Self–Trapped Excitons in Stable Sb^{3+}–Doped $Cs_2NaInCl_6$ Double Perovskites. *J. Phys. Chem. Lett*. **2020,** *11,* 6, 2053–2061.

(18) Noculak, A.; Morad, V.; McCall, K. M.; Yakunin, S.; Shynkarenko, Y.; Wörle, M.; Kovalenko, M. V. Bright Blue and Green Luminescence of Sb(III) in Double Perovskite (M = Na, K) Matrices. *Chem. Mater.* **2020,** *32,* 5118–5124.

(19) Majher, J. D.; Gray, M. B.; Strom, T. A.; Woodward, P. M. $Cs_2NaBiCl_6:Mn^{2+}$ – A New Orange–Red Halide Double Perovskite Phosphor. *Chem. Mater.* **2019,** *31,* 5, 1738–1744.

(20) Zhou, J.; Rong, X.; Zhang, P.; Molokeev, M. S.; Wei, P.; Liu, Q.; Zhang, X.; Xia, Z. Manipulation of Bi^{3+}/In^{3+} Transmutation and Mn^{2+}–Doping Effect on the Structure and Optical Properties of Double Perovskite $Cs_2NaBi_{1-x}In_xCl_6$. *Adv. Opt. Mater.* **2019,** *7*, 8, 1801435.

(21) Yao, M.; Wang, L.; Yao, J.; Wang, K.; Chen. C.; Zhu, B.; Yang, J.; Wang, J.; Xu, W.; Zhang, Q.; Yao, H. Improving Lead–Free Double Perovskite $Cs_2NaBiCl_6$ Nanocrystal Optical Properties via Ion Doping. *Adv. Opt. Mater.* **2020,** *8,* 8, 1901919.

(22) Zhao, F.; Song, Z.; Zhao, J.; Liu, Q. Double perovskite $Cs_2AgInCl_6:Cr^{3+}$: broadband and near–infrared luminescent materials. *Inorg. Chem. Front.* **2019,** *6,* 3621–3628.

(23) Luo, J.; Wang, X.; Li, S. *et al.* Efficient and stable emission of warm–white light from lead–free halide double perovskites. *Nature* **2018,** *563,* 541–545.

(24) Gray, M. B.; Majher, J. D.; Strom, T. A.; Woodward, P. M. Broadband White Emission in $Cs_2AgIn_{1-x}Bi_xCl_6$ Phosphors. *Inorg. Chem.* **2019,** *58,* 19, 13403–13410.

(25) Han, P.; Zhang, X.; Mao, X.; Yang, B.; Yang, S.; Feng, Z.; Wei, D>; Deng, W.; Pullerits, T.; Han, K. Size effect of lead–free halide double perovskite on luminescence property. *Sci. China Chem.* **2019,** *62,* 1405–1413.

(26) Ke, B.; Zeng, R.; Zhao, Z.; Wei, Q.; Xue, X.; Bai, K.; Cai, C.; Zhou, W.; Xia, Z.; Bingsuo, Z. Homo– and Heterovalent Doping–Mediated Self–Trapped Exciton Emission and Energy Transfer in Mn–Doped $Cs_2Na_{1-x}Ag_xBiCl_6$ Double Perovskites. *J. Phys. Chem. Lett.* **2020,** *11,* 1, 340–348.

(27) Tan, Z.; Li, J.; Zhang, C.; Li, Z.; Hu, Q.; Xiao, Z.; Kamiya, T.; Hosono, H.; Niu, G.; Lifshitz, E.; Cheng, Y.; Tang, J. Highly Efficient Blue–Emitting Bi–Doped Cs_2SnCl_6 Perovskite Variant: Photoluminescence Induced by Impurity Doping. *Adv. Funct. Mater.* **2018,** *28,* 1801131.

(28) Li, J.; Tan, Z.; Hu, M.; Chen, C.; Luo, J.; Li, S.; Gao, L.; Xiao, Z.; Niu, G.; Tang, J. Antimony doped Cs_2SnCl_6 with bright and stable emission. *Front. Optoelectron.* **2019,** *12,* 4, 352–364.

(29) Yan, A.; Li, K.; Zhou, Y.; Ye, Y.; Zhao, X.; Liu, C. Tuning the optical properties of Cs_2SnCl_6:Bi and Cs_2SnCl_6:Sb lead–free perovskites via post–annealing for white LEDs. *J. Alloys Compd.* **2020,** *822,* 153528.

(30) Jing, Y.; Liu, Y.; Zhao, J.; Xia, Z. Sb^{3+} Doping-Induced Triplet Self-Trapped Excitons Emission in Lead-Free Cs_2SnCl_6 Nanocrystals. *J. Phys. Chem. Lett.* **2019,** *10,* 23, 7439–7444.

(31) Jing, Y.; Liu, Y.; Jiang, X.; Molokeev, M. S.; Lin, Z.; Xia, Z. Sb^{3+} Dopant and Halogen Substitution Triggered Highly Efficient and Tunable Emission in Lead-Free Metal Halide Single Crystals. *Chem. Mater.* **2020,** *32,* 12, 5327-5334.

(32) Liu, X.; Xu, X.; Li, B.; Liang, Y.; Li, Q.; Jiang, H.; Xu, D. Antimony–Doping Induced Highly Efficient Warm–White Emission in Indium–Based Zero–Dimensional Perovskites. *CCS Chem.* **2020,** *2,* 216–224.

(33) Han, P.; Luo, C.; Yang, S.; Yang, Y.; Deng, W.; Han, K. All–Inorganic Lead–Free 0–D Perovskites Through Doping Strategy Achieving A Boost of PLQY from < 2% to 90%. *Angew. Chem. Int. Ed.* **2020.** (https://doi.org/10.1002/anie.202003234)

(34) *Topas Academic, General Profile and Structural Analysis for Powder Diffraction Data*; Bruker AXS: Karlsruhe, Germany, 2004.

(35) Momma, K.; Izumi, F. *VESTA 3* for three–dimensional visualization of crystal, volumetric and morphology data. *J. Appl. Cryst.* **2011,** *44,* 1272–1276.

(36) Amilius, Z.; van Laar, B; Rietveld, H. M. The crystal structure of K_3MoCl_6. *Acta Cryst.* **1969,** *B25,* 400–402.

(37) Goldschmidt, V. M. Die Gesetze der Krystallochemie. *Naturwissenschaften* **1926,** *14,* 477–485.

(38) Abakumov, A. M.; King, G.; Laurinavichute, V. K.; Rozova, M. G.; Woodward, P. M. Antipov, E. The Crystal Structure of α–K_3AlF_6: Elpasolites and Double Perovskites with Broken Corner–Sharing Connectivity of the Octahedral Framework. *Inorg. Chem.* **2009,** *48,* 9336–9344.

(39) Ranfagni, A.; Mugani, D.; Bacci, M.; Viliani, G.; Fontana, M. P. The optical properties of thallium–like impurities in alkali–halide crystals. *Adv. Phys.* **1983,** *32*, 6, 823–905.

(40) Blasse, G.; Grabmaier, B. B. *Luminescent Materials;* Springer Verlag: Heidelberg, Germany, 1994.

(41) Wang, L.; Li, H.; Guo, Y.; Jiang, H.; Wang, Q.; Ren, C.; Shi, J. Design and Synthesis of $CdWO_4:Sb^{3+}$ Phosphor Based on *sp* Energy Level Regularities of Sb^{3+} Ion. *J. Am. Ceram. Soc.* **2015,** *98,* 7, 2146–2152.

(42) Gislason, J.; Lloyd, M. H.; Tuck, D. G. Coordination Compounds of Indium. X. Anionic Indium(III) Halide Complexes. *Inorg. Chem.* **1971,** *10,* 1907–1910.

(43) Benachenhou, F. Mairesse, G.; Nowogrocki, G.; Thomas, D. Structural Studies of Cs–K–Bi Mixed Chlorides Relation to the Crystal Structures of A_2BMX_6, A_3MX_6, and A_2MX_6. *J. Solid State Chem.* **1986,** *65,* 13–26.

(44) McCall, K.; Friedrich, D.; Chica, D. G.; Cai, W.; Stoumpos, C. C.; Alexander, G. C. B.; Deemyad, S.; Wessels, B. W.; Kanatzidis, M. G. Perovskites with a Twist: Strong In^{1+} Off–Centering in the Mixed–Valent $CsInX_3$ (X = Cl, Br). *Chem. Mater.* **2019,** *31,* 22, 9554–9566.

(45) King, G.; Abakumov, A. M.; Hadermann, J.; Alekseeva, A. M.; Rozova, M. G.; Perkisas, T.; Woodward, P. M.; Tendeloo, G. V.; Antipov, E. V. Crystal Structure and Phase Transitions in Sr_3WO_6. *Inorg. Chem.* **2010,** *49,* 6058–6065.

(46) King, G.; Abakumov, A. M.; Woodward, P. M.; Llobet, A.; Tsirlin, A. A.; Batuk, D.; Antipov, E. V. The High–Temperature Polymorphs of K_3AlF_6. *Inorg. Chem.* **2011**, *50*, 7792–7801.

(47) Fry, A. M.; Woodward, P. M. Structures of α–$K_3MoO_3F_3$ and α–$Rb_3MoO_3F_3$: Ferroelectricity from Anion Ordering and Noncooperative Octahedral Tilting. *Cryst. Growth Des.* **2013,** *13,* 5405–5410.

(48) Barbier, P.; Drache, M.; Mairesse, G.; Ravez, J. Properties of bismuth halides with $(NH_4)_3FeF_6$ or K_2NaAlF_6 related structure. *Ferroelectrics* **1984,** *55,* 113–116.

(49) Mattfeld, H.; Meyer, G. A_3YCl_3 (A = K, NH_4, Rb, Cs): Synthese, Stukturen, Thermisches Verhalten. Uber einige analoge Chloride der Lanthanide. *Z. anorg. allg. Chem.* **1992,** *618,* 13–17.

(50) Oomen, E. W. J. L.; Smit, W. M. A.; Blasse, G. On the luminescence of Sb^{3+} in Cs_2NaMCl_6 (with M=Sc,Y,La): a model system for the study of trivalent s^2 ions. J. Phys. C: Solid State Phys. **1986,** *19,* 3263–3272.

(51) Blasse, G.; Dirksen, G. J.; Abriel, W. The influence of distortion of the Te(IV) coordination octahedron on its luminescence. *Chem. Phys. Lett.* **1987,** *136,* 460–464.

(52) Gundiah, G.; Brennan, K.; Yan, Z.; Samulon, E. C.; Wu, G.; Bizarri, G. A.; Derenzo, S. E.; Bourret–Courchesne E. D. Structure and scintillation properties of Ce^{3+}–activated $Cs_2NaLaCl_6$, Cs_3LaCl_6, $Cs_2NaLaBr_6$, Cs_3LaBr_6, Cs_2NaLaI_6 and Cs_3LaI_6. *J. Lumin.* **2014,** *149,* 374–384.

(53) Hinz, D.; Gloger, T.; Meyer, G. Kristallstrukturen von Na_3TiCl_6 und K_3TiCl_6. *Z. anorg. allg. Chem.* **2000,** *626,* 822–824.

(54) Černý, R.; Ravnsbæk, D. B.; Severa, G.; Filinchuk, Y.; D' Anna, V.; Hagemann, H.; Haase, D.; Skibsted, J.; Jensen, C. M.; Jensen, T. R. Structure and Characterization of $KSc(BH_4)_4$. *J. Phys. Chem. C* **2010,** *114,* 45, 19540−19549.

(55) Ward, M.D.; Ibers, J. A. Cs_3ScCl_6. *Acta Cryst*. **2014,** *E70,* i25.

(56) Chen, L.; Wu, B. –L.; He, X. –Y.; Mi, J –X. A monoclinic modification of $K_3[InCl_6]$. *Acta Cryst.* **2006,** *E62,* i143–i144.

(57) Mattfeld, H.; Meyer, G. Ternäre Halogenide vom Typ A_3MX_6. A_3YCl_6 (A = K, NH_4, Rb, Cs): Synthese, Strukturen, Thermisches Verhalten. Über einige analoge Chloride der Lanthanide. *Z. anorg. allg. Chem.* **1992,** *618,* 13–17.

(58) Seifert, H. J.; Fink, H.; Baumgartner, B. Structure and Stability of the Low-Temperature Modification of Compounds Cs_3LnCl_6 (Ln = La-Gd). *J. Solid State Chem.* **1993,** *107,* 19–26.

(59) Lazarini, F. Rubidium hexabromobismuthate(III). *Acta Cryst.* **1978,** *B34,* 2288–2290.

(60) Tang, Y.; Liang, M.; Chang, B.; Sun, H.; Zheng, K.; Pullerits, T.; Chi, Q. Lead-free double halide perovskite Cs_3BiBr_6 with well-defined crystal structure and high thermal stability for optoelectronics. *J. Mater. Chem. C* **2019,** *7,* 3369–3374.

TOC Synopsis:

Rb_3InCl_6 is prepared through a conversion of $Rb_2InCl_5 \cdot H_2O$ in acetonitrile. Rb_3InCl_6 crystallizes in the *C*2/*c* space group and contains isolated $[InCl_6]^{3-}$ octahedra surrounded by Rb^+ ions. The structure is related to cubic double perovskites through noncooperative tilting of $[InCl_6]^{3-}$ octahedra. Partial replacement of In^{3+} for Sb^{3+} results in bright cyan-green photoluminescence (λ_{max} = 522 nm), originating from transitions localized on isolated $[SbCl_6]^{3-}$ octahedra, thus demonstrating the potential of A_3MX_6 halides for photoluminescent applications.